

LAViG-FLOW: Latent Autoregressive Video Generation for Fluid Flow Simulations

V. De Pellegrini¹, T. Alkhalifah¹

¹Earth Science and Engineering Program, Physical Science and Engineering Division, King Abdullah University of Science and Technology (KAUST), Thuwal, 23955-6900, Kingdom of Saudi Arabia

Key Points:

- Dedicated autoencoders learn carbon dioxide saturation and pressure build-up fields. Their latents feed a video diffusion transformer model.
- This video diffusion transformer model learns their coupled distribution, and shows autoregressive prediction capability.
- We demonstrate that this diffusion pipeline runs orders of magnitude faster than traditional numerical reservoir solvers.

Abstract

Modeling and forecasting subsurface multiphase fluid flow fields underpin applications ranging from geological CO₂ sequestration (GCS) operations to geothermal production. This is essential for ensuring both operational performance and long-term safety. While high fidelity multiphase simulators are widely used for this purpose, they become prohibitively expensive once many forward runs are required for inversion purposes and quantify uncertainty. To tackle this challenge we propose LAViG-FLOW, a latent autoregressive video generation diffusion framework that explicitly learns the coupled evolution of saturation and pressure fields. Each state variable is compressed by a dedicated 2D autoencoder, and a Video Diffusion Transformer (VDiT) models their coupled distribution across time. We first train the model on a given time horizon to learn their coupled relationship and then fine-tune it autoregressively so it can extrapolate beyond the observed time window. Evaluated on an open-source CO₂ sequestration dataset, LAViG-FLOW generates saturation and pressure fields that stay consistent across time while running orders of magnitude faster than traditional numerical solvers.

Plain Language Summary

Subsurface energy operations such as geological CO₂ sequestration, geothermal production, and hydrogen storage inject fluids into porous rock layers, driving multiphase flow through the connected pore network. These injections change how much pore space is filled (saturation) and how strongly the fluid pushes on the rock (pressure build-up), so engineers must track both fields to avoid fractures or leakage. Traditional reservoir simulators are used to model these coupled effects but are computationally expensive. Because of this, we rely on artificial intelligence and design an alternative to these conventional tools. We build a deep learning workflow, specifically a generative modeling framework, that produces videos of how saturation and pressure fields evolve during CO₂ injection into reservoir formations. We demonstrate that it runs faster than petroleum industry reservoir simulators.

1 Introduction

Modeling and forecasting subsurface multiphase fluid flow fields are needed across a wide range of energy and environmental applications, ranging from geological CO₂ sequestration to geothermal production and hydrogen storage. Accurately monitoring subsurface saturation and pressure evolution is therefore critical for safety and long-term containment. Among these efforts, geological CO₂ sequestration (GCS) draws particular focus because it is a promising strategy to mitigate atmospheric carbon emissions. Supercritical CO₂ is injected into saline aquifers or depleted hydrocarbon formations, migrates under buoyancy, capillarity, and viscous forces, and eventually becomes immobilized via structural, residual, solubility, and mineral trapping mechanisms (Bachu, 2008; Lee et al., 2016; Saadatpoor et al., 2010; Krevor et al., 2015).

A conventional numerical simulator, which solves multiphase Darcy flow equations across high-resolution spatial and temporal grids, remains the most robust and widely used tool for predicting subsurface plume migration and pressure evolution (Pruess et al., 1999; Zhao et al., 2023). However, its application to realistic scenarios is limited by high computational cost, particularly when multiple realizations are required to do inversion and prediction, as well as quantify the uncertainty involved (Nordbotten et al., 2012; Gan et al., 2021).

In the era of artificial intelligence, deep learning models can substitute these costly simulators. While preserving the underlying physics, they can significantly reduce runtime. There are several examples in the literature; among them are transformer-based architectures like TransUNet (Tariq et al., 2023), neural operators such as U-FNO and

MIONet (Wen et al., 2022b; Jin et al., 2022), and enhanced DeepONets (Diab & Al Kobaisi, 2024), which learn complex deterministic mappings from numerical simulator inputs to dynamic field responses.

Here, we explore the use of diffusion models, especially video diffusion models (Ho et al., 2022a), which can address the same task while learning stochastic spatio-temporal data distributions instead of deterministic mappings. X. Huang et al. (2024) first proposed a toy example showing how a diffusion model can store the distribution of subsurface elastic-property changes induced by CO₂ injection. Building on this, we introduce LAViG-FLOW, a latent autoregressive video diffusion framework whose DiT backbone builds upon Ma et al. (2024) and learns the coupled evolution of CO₂ gas saturation and pressure build-up fields for CO₂ injection scenarios within heterogeneous 2D radially symmetric reservoirs (Figure 1).

1.1 Key Contributions

- We formulate separate latent spaces for physically related state variables, CO₂ gas saturation and pressure build-up, via dedicated 2D Vector Quantized Variational Autoencoder (2D VQ-VAE) and 2D Variational Autoencoder (2D VAE), concatenating their outputs into a shared latent representation for the video diffusion model.
- We train a single Video Diffusion Transformer (ViDT) on the shared latent representation formed by concatenating the CO₂ gas saturation and pressure build-up encodings; we demonstrate that this model learns their joint distribution and, after autoregressive fine-tuning, generalizes beyond the training horizon while keeping the outputs physically consistent.
- We demonstrate that our diffusion pipeline runs orders of magnitude faster than traditional numerical reservoir solvers.
- The proposed diffusion pipeline is flexible enough to accept different input sizes and incorporate additional physically related field variables.

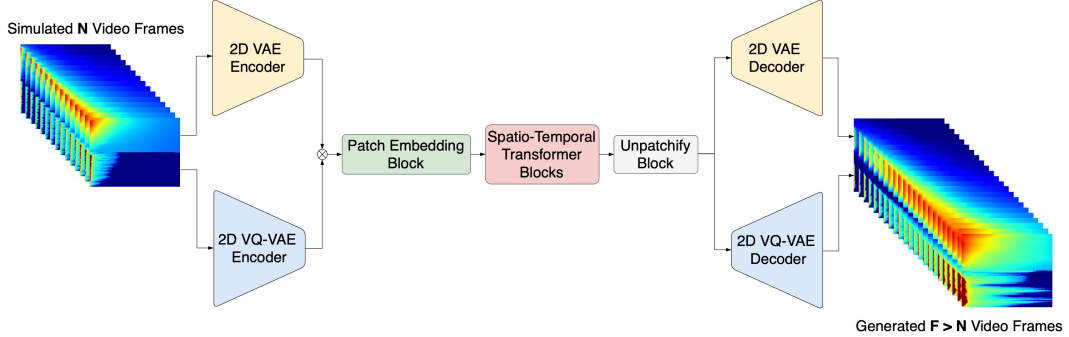


Figure 1. Overview of the LAViG-FLOW pipeline: A reservoir simulator provides N video frames of CO₂ gas saturation and corresponding pressure build-up fields, which are first compressed via 2D VQ-VAE and 2D VAE encoders, concatenated, patch-embedded, and passed through spatio-temporal Transformer blocks before being unpatchified; the VQ-VAE decoder recovers CO₂ gas saturation and the VAE decoder recovers pressure build-up, so the pipeline generates $F > N$ video frames at inference.

2 Related Work

2.1 Video Generative Models

Video generative models have recently achieved remarkable success at generating high quality videos. There are several types of video prediction models that can be dis-

tinguished according to their backbone architecture, the dimensional space they operate in, whether they are conditioned and on what kind of conditioning, and other design and training choices. We span this spectrum starting with video predictors that include generative adversarial networks (Goodfellow et al., 2014) and ending with models that rely on diffusion transformer (DiT) architectures (Peebles & Xie, 2022) such as those described as Latte (Ma et al., 2024) and DiTPainter (Chen et al., 2024). We likewise move from pixel space predictors (Babaeizadeh et al., 2021) toward latent space models (Blattmann, Dockhorn, et al., 2023; Blattmann, Rombach, et al., 2023). Pixel space predictors can rely on reconstruction guidance to extend the generation horizon for autoregressive prediction (Ho et al., 2022b), and latent space models can rely on autoregressive strategies for long video generation (Y. Zhang et al., 2024; J. Liu et al., 2024). Conditioning can come from text prompts (He et al., 2022), 2D scenes (H.-P. Huang et al., 2024), or other modalities, and many additional hybrids continue to appear.

2.2 Video Diffusion Models for Subsurface CO₂ Plumes

In the field of subsurface fluid flow the only video diffusion example we are aware of is provided by X. Huang et al. (2024), who reuse Ho et al. (2022b)'s reconstruction guided pixel space formulation to learn the distribution of elastic-property changes due to CO₂ injection. However, their method operates on fixed low resolution 64 × 64 input frames, works entirely in pixel space, and relies on reconstruction guidance to forecast very short horizons (roughly one additional year) based on early history frames, while evaluation is limited to synthetic, simple scenarios. By contrast, we propose a high resolution latent VDiT model whose backbone architecture is taken from Ma et al. (2024) to specifically learn the distribution of CO₂ gas saturation and pressure build-up field variables. The model can accept arbitrary input sizes thanks to its latent space representation and is fine-tuned with autoregressive strategies (Y. Zhang et al., 2024; J. Liu et al., 2024) to generate far-in-the-future frames conditioned on flexible length histories. In addition, our conditioning scheme allows us to choose how many history frames and how many future frames to produce. Finally, the model is evaluated on synthetic data of resolution 96 × 200 that cover a broad range of realistic GCS scenarios (Wen et al., 2022b).

3 Preliminaries

3.1 Autoregressive Video Prediction Model

We aim to learn a video prediction model that outputs future frames $x_{c:F'} = (x_c, \dots, x_{F'-1})$ with $F' > F$, conditioned on the first c frames $x_{<c} = (x_0, \dots, x_{c-1})$ of a video $x_{0:F-1} = (x_0, \dots, x_{F-1})$, where $\mathbf{x}_f \in \mathbb{R}^{H \times W \times N_{\text{ch}}}$ is the frame at timestep f (J. Liu et al., 2024; Weissenborn et al., 2020). The conditional distribution $p(x_{c:F'} | x_{<c})$ is determined autoregressively in the latent space to accelerate runtime.

3.2 Variational Autoencoder

VAE (Kingma & Welling, 2022; Higgins et al., 2017) pairs an encoder that compresses images into continuous latent representations with a decoder that reconstructs the same image from those latent representations. Given a pressure build-up image $x \in \mathbb{R}^{H \times W \times N_{\text{ch}}}$, the encoder E maps it to $z \in \mathbb{R}^{H' \times W' \times N_z}$ and the decoder D reconstructs it. The VAE is trained by minimizing the following objective function:

$$\mathcal{L}_{\text{VAE}}(x) = \underbrace{\mathbb{E}_{q_{\phi}(z|x)} \|\mathcal{D}_{\theta}(z) - x\|_2^2}_{\mathcal{L}_{\text{recon}}} + \beta \underbrace{D_{\text{KL}}(q_{\phi}(z|x) \parallel \mathcal{N}(0, \mathbf{I}))}_{\mathcal{L}_{\text{KL}}}, \quad (1)$$

where $\mathcal{L}_{\text{recon}}$ is the reconstruction loss that measures the distance between the original input x and its reconstruction $\mathcal{D}_{\theta}(z)$; the expectation $\mathbb{E}[\cdot]$ inside $\mathcal{L}_{\text{recon}}$ is taken over the

encoder distribution $q_\phi(z \mid x)$. \mathcal{L}_{KL} is the Kullback–Leibler divergence loss weighted by β , regularizing that encoder distribution toward $\mathcal{N}(0, \mathbf{I})$.

3.3 Vector Quantized Variational Autoencoder

The VQ-VAE (van den Oord et al., 2017) pairs an encoder that compresses images into discrete latent representations with a decoder that reconstructs the same image from those latent representations. Given a CO_2 gas saturation image $x \in \mathbb{R}^{H \times W \times N_{\text{ch}}}$, the encoder E produces a feature map $z_e(x) \in \mathbb{R}^{H' \times W' \times N_z}$ with spatial size $H' \times W'$. Each of the $H'W'$ spatial locations is a latent vector $z_j(x) \in \mathbb{R}^{N_z}$ for $j = 1, \dots, H'W'$. A codebook $\mathcal{C} = \{e_k\}_{k=1}^K$ stores discrete vectors $e_k \in \mathbb{R}^{N_z}$; each latent vector is replaced with its nearest codebook entry, producing the quantized sequence $z_q(x) = (e_{q(x,1)}, \dots, e_{q(x,H'W')})$ that the decoder G uses to reconstruct $\hat{x} = G(z_q(x))$. The VQ-VAE is trained by minimizing the following objective:

$$\mathcal{L}_{\text{VQ-VAE}}(x) = \underbrace{\|x - G(z_q(x))\|_2^2}_{\mathcal{L}_{\text{recon}}} + \underbrace{\|\text{sg}[z_e(x)] - z_q(x)\|_2^2}_{\mathcal{L}_{\text{codebook}}} + \beta \underbrace{\|\text{sg}[z_q(x)] - z_e(x)\|_2^2}_{\mathcal{L}_{\text{commit}}}, \quad (2)$$

where $\mathcal{L}_{\text{recon}}$ is again the reconstruction loss, $\mathcal{L}_{\text{codebook}}$ pulls the codebook entries toward the encoder outputs, and $\mathcal{L}_{\text{commit}}$ keeps the encoder stable by encouraging $z_e(x)$ to stay close to the selected code vectors; $\text{sg}[\cdot]$ is the stop-gradient operator that blocks gradients where needed. An optional LPIPS perceptual term $\mathcal{L}_{\text{LPIPS}}$ (R. Zhang et al., 2018; Johnson et al., 2016) penalizes high-level discrepancies between x and $G(z_q(x))$.

4 Method

We present the workflow adopted to train the LAViG-FLOW pipeline (Figure 1), which comprises 2 training stages followed by a fine-tuning stage.

4.1 Stage I: Dual 2D Autoencoder Training

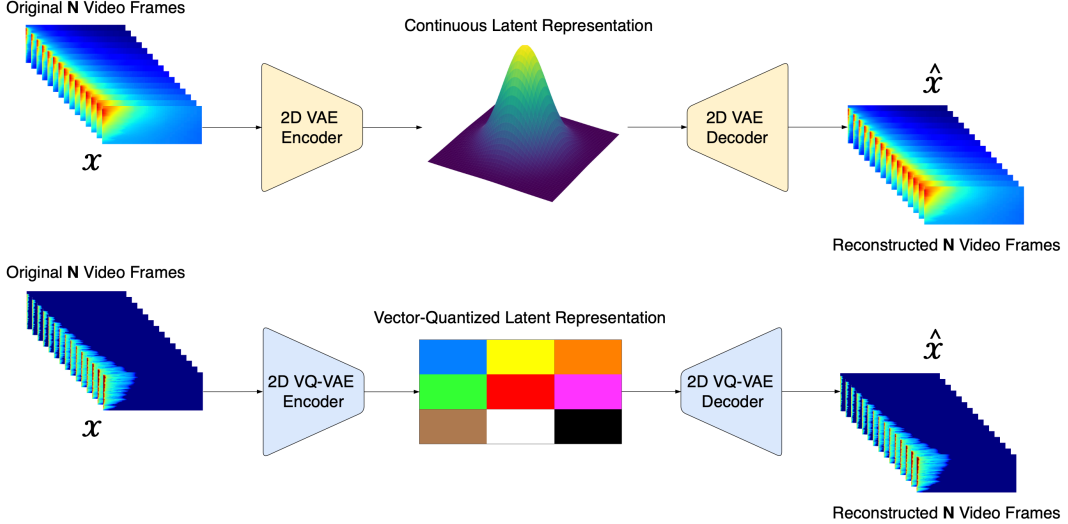


Figure 2. Training workflow for **Stage I**: the pressure build-up images are compressed into a continuous latent representation, while the CO_2 gas saturation images are compressed into a vector-quantized latent representation. Here, \mathbf{x} denotes the input frames and $\hat{\mathbf{x}}$ denotes the reconstructed frames after decoding.

Figure 2 summarizes the dual path setup used at this stage. We utilize 2D VQ-VAE and VAE models to generate the latent representation for CO_2 gas saturation and pressure build-up videos, respectively. Each video clip of length F is reshaped from $\mathbb{R}^{B \times F \times N_{\text{ch}} \times H \times W}$

to $\mathbb{R}^{(B \cdot F) \times N_{\text{ch}} \times H \times W}$; modeling temporal dynamics is left for later diffusion stages. The models are trained using the losses described in Section 3.

4.2 Stage II: Latent Video Diffusion Transformer Model Pre-Training

Figure 3 summarizes the pre-training workflow of this stage. We pre-train a single latent VDiT model (Ma et al., 2024) to capture the joint distribution of CO₂ gas saturation and pressure build-up clips of length F . The input is assembled by concatenating the latents of CO₂ gas saturation $z_{\text{gas}} \in \mathbb{R}^{(B \cdot F) \times N_{z_{\text{gas}}} \times H' \times W'}$ and pressure build-up $z_{\text{pressure}} \in \mathbb{R}^{(B \cdot F) \times N_{z_{\text{pressure}}} \times H' \times W'}$ along the channel dimension, yielding $z \in \mathbb{R}^{(B \cdot F) \times (N_{z_{\text{gas}}} + N_{z_{\text{pressure}}}) \times H' \times W'}$. We reshape z into $z \in \mathbb{R}^{B \times F \times (N_{z_{\text{gas}}} + N_{z_{\text{pressure}}}) \times H' \times W'}$ and feed it to a patch embedding block where every frame is patchified using the uniform frame patch embedding strategy from ViT (Dosovitskiy et al., 2021). The resulting tokens are projected to a hidden dimension D and processed by a DiT-style backbone that alternates spatial and temporal self-attention blocks (Variant I) (Ma et al., 2024), with AdaLN-Zero conditioning in each block (Peebles & Xie, 2022). After the transformer blocks, tokens are unpatchified into latent frames and decoded back to pixel space. We train the diffusion framework as follows. During the forward diffusion process, we corrupt each clip by sampling $\epsilon \sim \mathcal{N}(0, \mathbf{I})$, defining $\alpha(t) = 1 - t/T$ for $t \sim \mathcal{U}(0, T)$ with $T = 1,000$, and setting $z_t = \alpha(t) z_0 + (1 - \alpha(t)) \epsilon$. The VDiT then produces two output groups per frame, and we interpret the first group as the velocity field $v_\theta = f_\theta(z_t, t) \in \mathbb{R}^{B \times F \times C \times H' \times W'}$, where $C = N_{z_{\text{gas}}} + N_{z_{\text{pressure}}}$, which we regress toward the clean-minus-noise target:

$$\mathcal{L}_{\text{RF}} = \mathbb{E}[\|v_\theta - (z_0 - \epsilon)\|_2^2], \quad (3)$$

averaged over spatial and temporal positions; $\mathbb{E}[\cdot]$ denotes the expectation. During the reverse denoising process, the injected noise is iteratively removed by the VDiT predictor, and the reconstruction is implemented via a 30-step sampler that follows rectified-flow theory (M. Liu et al., 2023; X. Liu et al., 2022; Kim et al., 2025), instead of the 1,000-step DDPM schedule of Ho et al. (2020).

4.3 Stage III: Autoregressive Latent Video Diffusion Transformer Model Fine-Tuning

Figure 3 also summarizes the autoregressive fine-tuning workflow. We fine-tune the pre-trained VDiT model to extend the learned distribution of length F videos to longer horizons $F' > F$ for autoregressive prediction. To do this, we define the number of F_c context frames and the number of F_p prediction frames. The context frames represent the observation history, referring to frames within the learned horizon F during Stage II in which the model was trained on, while the prediction frames are those generated beyond the training horizon F . We follow the strategy proposed in J. Liu et al. (2024) and Y. Zhang et al. (2024). Specifically, context latent frames are concatenated with zero initialized placeholders and processed by the VDiT under a binary mask $m \in \{0, 1\}^{B \times F}$ that enforces $\mathbf{z}_t \leftarrow m \odot \mathbf{z}_t + (1 - m) \odot \mathbf{z}_0$, where \odot denotes the elementwise product, so that context frames stay noise free and only the prediction frames receive noise. This yields a sliding, overlapping procedure: each step treats F_c frames as known and predicts F_p , then shifts so the newest F_c frames, combining the recent predictions with the last portion of the preceding context, form the next context window.

5 Experiments

We design our experiments to address the following questions:

- Can LAViG-FLOW learn the joint distribution of physically coupled state variables (e.g., CO₂ gas saturation and pressure build-up)?

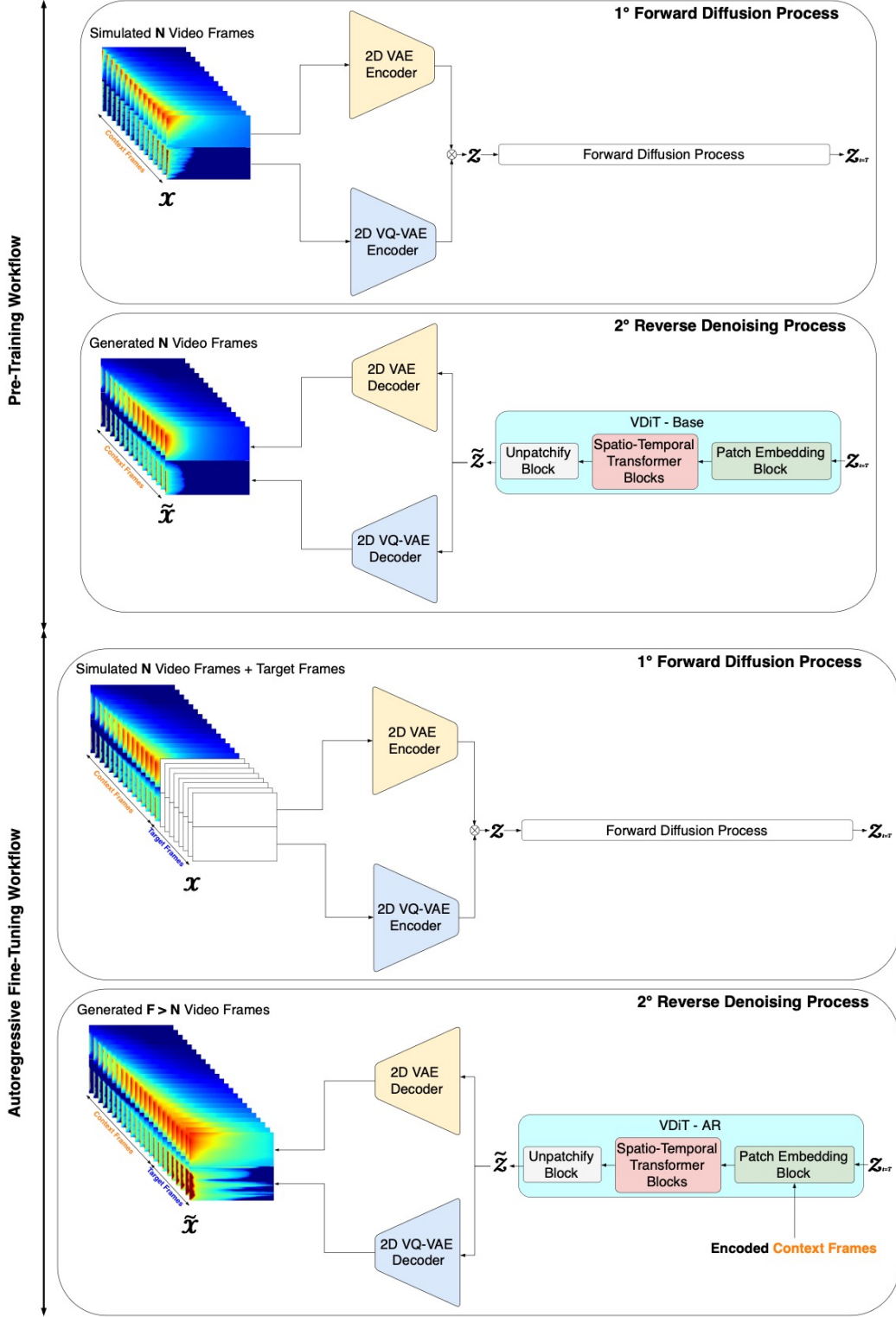


Figure 3. Stage II (pre-training): Gaussian noise is used to corrupt the joint latent video and VDiT-Base removes it; at inference, VDiT-Base denoises Gaussian noise into an N -frame video (same length as input). **Stage III (autoregressive fine-tuning):** The same workflow is fine-tuned into VDiT-AR (autoregressive) to predict future frames from N context frames, yielding $F > N$ frames; inference is unconditional (start from noise) or conditional (fix encoded context frames). Symbols: x is the input clip of length N (context frames only, Stage II) or $N +$ target frames (Stage III); z concatenated latents; $z_{t=T}$ fully noised latents at step ($t=T$); \tilde{z} denoised latents; \tilde{x} decoded clip of length N (Stage II) or $F > N$ (Stage III).

- Assuming that the answer to the first question is positive, can LAViG-FLOW extrapolate beyond the training horizon via progressive autoregression while maintaining physical consistency?

5.1 Implementation

We train with HuggingFace Accelerate on a GPU cluster (dual Intel® Xeon® compute nodes equipped with NVIDIA Tesla V100 GPUs). In Stage I we use 8 V100 GPUs to train the VQ-VAE for 60 epochs with an Adam optimizer at a learning rate of 1×10^{-5} and the VAE for 300 epochs with an Adam optimizer at a learning rate of 1×10^{-4} . Both encoders downsample the spatial dimensions by a factor $f = \frac{H}{h} = \frac{W}{w} = 8$ and are frozen for later stages. The VQ-VAE has 3 stride-2 down blocks, 1 mid block, and 3 up blocks (channels 256 \rightarrow 384 \rightarrow 512 \rightarrow 1024); each block contains 2 residual sub-blocks with convolutions, group norm (32 groups), and SiLU activations, and there are no attention layers. The codebook size is 16,384, and the latent channels $z_{\text{gas}} = 2$. The VAE mirrors this layout with 3 stride-2 down blocks, one mid block, and 3 up blocks (channels 32 \rightarrow 64 \rightarrow 128 \rightarrow 128); each block has 1 residual sub-block with convolutions, group norm (16 groups), and SiLU activations, and no attention layers. Latent channels are $z_{\text{pressure}} = 24$ (mean/variance are predicted jointly). Stage II pre-trains the VDiT for 1,000 epochs using an AdamW optimizer with a learning rate of 3×10^{-5} , gradient accumulation = 1, the 30-step rectified-flow loss described in Section 4, a uniform 2 \times 2 frame patch embedding, and hidden dimension $D = 512$. Stage III fine-tunes the same backbone for 400 epochs with an autoregressive strategy. Both diffusion stages run on 6 V100 GPUs, and share the VDiT backbone (38,890,192 parameters): 8 transformer layers arranged as alternating spatial and temporal DiT attention blocks (each attention block uses 8 heads with head dimension 64), and timestep embeddings of size 256.

5.2 Setup

We evaluate on the open-source CO₂ sequestration dataset (Wen et al., 2022a). The dataset is generated with ECLIPSE (E300) simulator on a 2D radially symmetric reservoir of radius 100 km and discretization 96 \times 200 (vertical \times radial), yielding the corresponding 12 \times 25 latent grid. Each simulation models 30 years of continuous CO₂ injection at a central vertical well ($r = 0.1$ m) under no-flow vertical boundaries and infinite-acting lateral boundaries. The simulator outputs CO₂ gas saturation and pressure build-up fields over 24 logarithmically spaced timesteps; we use the first 17 frames across all stages (I–III). The full dataset contains 5,500 simulations split into 4,500/500/500 train/validation/test samples. Stage I trains the autoencoders to produce latents for those 17 frames of CO₂ saturation and pressure build-up. Stage II pre-trains the VDiT to generate 17-frame videos. In Stage III we set $F_c = 15$ context frames drawn from the same 17 frames and predict $F_p = 2$ frames per step; this iterative scheme pushes forecasts beyond the training horizon. In addition, at inference we run 4 progressive steps: after providing $F_c = 15$ context frames, stages 1–4 predict 2, 4, 6, and 8 frames, yielding 23 frames in total. We compare these predicted frames against the validation dataset to verify consistency.

5.3 Qualitative Analysis

Figure 4 shows 21 unconditionally generated videos by the VDiT (Stage II), each depicting CO₂ saturation and pressure build-up over 17 frames. Figure 5 (Stage III) presents 19 unconditionally generated predictions using the autoregressive strategy. Figure 6 (Stage III inference) plots 3 sampled videos conditioned on $F_c = 15$ frames; stages 1–4 predict 2, 4, 6, and 8 frames (23 total), and we compare the predictions with the corresponding ground truths. By visually inspecting the generated videos we can make the following observations. For Stage II, the unconditionally generated videos exhibit smooth radial plume expansion and both CO₂ saturation and pressure build-up fields evolve together, con-

firming the hidden correspondence learned during joint training; all scenarios match the training setup, with injections starting on the left side where the well is located. Moving to Stage III, the autoregressive strategy extends this behavior beyond frame 17 without breaking the link between the two fields, and the red-labelled frames remain coherent with their preceding histories. Finally, the Stage III conditional results confirm that, with 15 observed frames, the predicted frames closely match the ground-truth validation clips, with no significant discrepancies between predictions and references.

5.4 Quantitative Analysis

We report Stage III inference results with $F_c = 15$ context frames across 4 stages, predicting $F_p \in \{2, 4, 6, 8\}$ frames per stage. The resulting clips are 17, 19, 21, and 23 frames long. Tables 1 and 2 summarize reconstruction errors (MSE, mean squared error; MAE, mean absolute error; RMSE, root mean squared error) and video quality metrics (SSIM, structural similarity; PSNR, peak signal-to-noise ratio; LPIPS, learned perceptual image patch similarity; FVD, Fréchet video distance) for both CO_2 gas saturation and pressure build-up. As F_p increases, performance naturally drops, yet errors grow steadily and remain bounded, indicating that the autoregressive strategy avoids abrupt drift. Table 3 reports approximate generation time per stage on a $1 \times$ NVIDIA V100 GPU, a $1 \times$ CPU (1 core), and a $1 \times$ CPU (4 cores).

Table 1. Reconstruction metrics averaged over 500 validation videos; best values per metric are highlighted in bold.

Stage	Pred. frames	CO ₂ Gas Saturation			Pressure Build-Up		
		MSE↓	MAE↓	RMSE↓	MSE↓	MAE↓	RMSE↓
1	2	0.001535 ± 0.001834	0.007593 ± 0.005329	0.034466 ± 0.018632	0.000940 ± 0.001517	0.010392 ± 0.008744	0.024830 ± 0.017980
2	4	0.002754 ± 0.003046	0.010643 ± 0.007168	0.046782 ± 0.023771	0.001686 ± 0.002483	0.014250 ± 0.012600	0.033583 ± 0.023634
3	6	0.004457 ± 0.004584	0.014168 ± 0.009333	0.060034 ± 0.029208	0.002864 ± 0.004082	0.019146 ± 0.016618	0.044054 ± 0.030381
4	8	0.006750 ± 0.006745	0.018425 ± 0.012152	0.074236 ± 0.035207	0.004624 ± 0.006594	0.025081 ± 0.021908	0.056482 ± 0.037867

Table 2. Video quality metrics averaged over 500 validation videos; best values per metric are highlighted in bold.

Stage	Pred. frames	CO ₂ Gas Saturation			Pressure Build-Up				
		SSIM↑	PSNR↑	LPIPS↓	FVD↓	SSIM↑	PSNR↑	LPIPS↓	FVD↓
1	2	0.975930 ± 0.021077	35.365925 ± 4.718784	0.022635 ± 0.017042	2.662165 ± 0.000000	0.982947 ± 0.030614	39.128849 ± 6.098355	0.023597 ± 0.024557	0.899850 ± 0.000000
2	4	0.959621 ± 0.033509	31.419082 ± 4.514989	0.039182 ± 0.026934	6.225822 ± 0.000000	0.971416 ± 0.042239	35.467971 ± 6.203071	0.031298 ± 0.032306	1.313972 ± 0.000000
3	6	0.938537 ± 0.050023	28.506753 ± 4.378120	0.057042 ± 0.037415	7.180684 ± 0.000000	0.953147 ± 0.057751	32.281777 ± 6.385572	0.045493 ± 0.044619	2.332940 ± 0.000000
4	8	0.909094 ± 0.074901	26.115507 ± 4.230447	0.077476 ± 0.048501	11.851633 ± 0.000000	0.927854 ± 0.076077	29.217962 ± 6.142253	0.063788 ± 0.054780	3.159044 ± 0.000000

Table 3. Approximate generation time per video.

Stage	Pred. frames	Video length (time frames)	V100 (s)	CPU 1 core (s)	CPU 4 cores (s)
1	2	17	0.63	83	23
2	4	19	0.93	113	33
3	6	21	1.23	153	43
4	8	23	1.53	173	53

6 Discussion & Future Work

Finally, we share the limitations of the approach and possible extensions. First, each temporal attention layer in the VDiT uses fixed absolute positional embeddings: it knows frame 2 follows frame 1, but it is not aware that frame 2 might correspond to “year 5.” Switching to rotary positional embeddings would let us express time offsets between frames and request a specific time frame (e.g., “generate year 10”).

Second, we evaluate on a sparse set of timesteps: frames are far apart in time, so the model misses the step by step evolution of CO_2 saturation and pressure. Denser time sampling would reveal the coupled dynamics more clearly and help the model learn them. Conditioning is also limited to historical context frames, leaving additional physics unmodeled. A planned extension involves conditioning on physical controls (e.g., injection

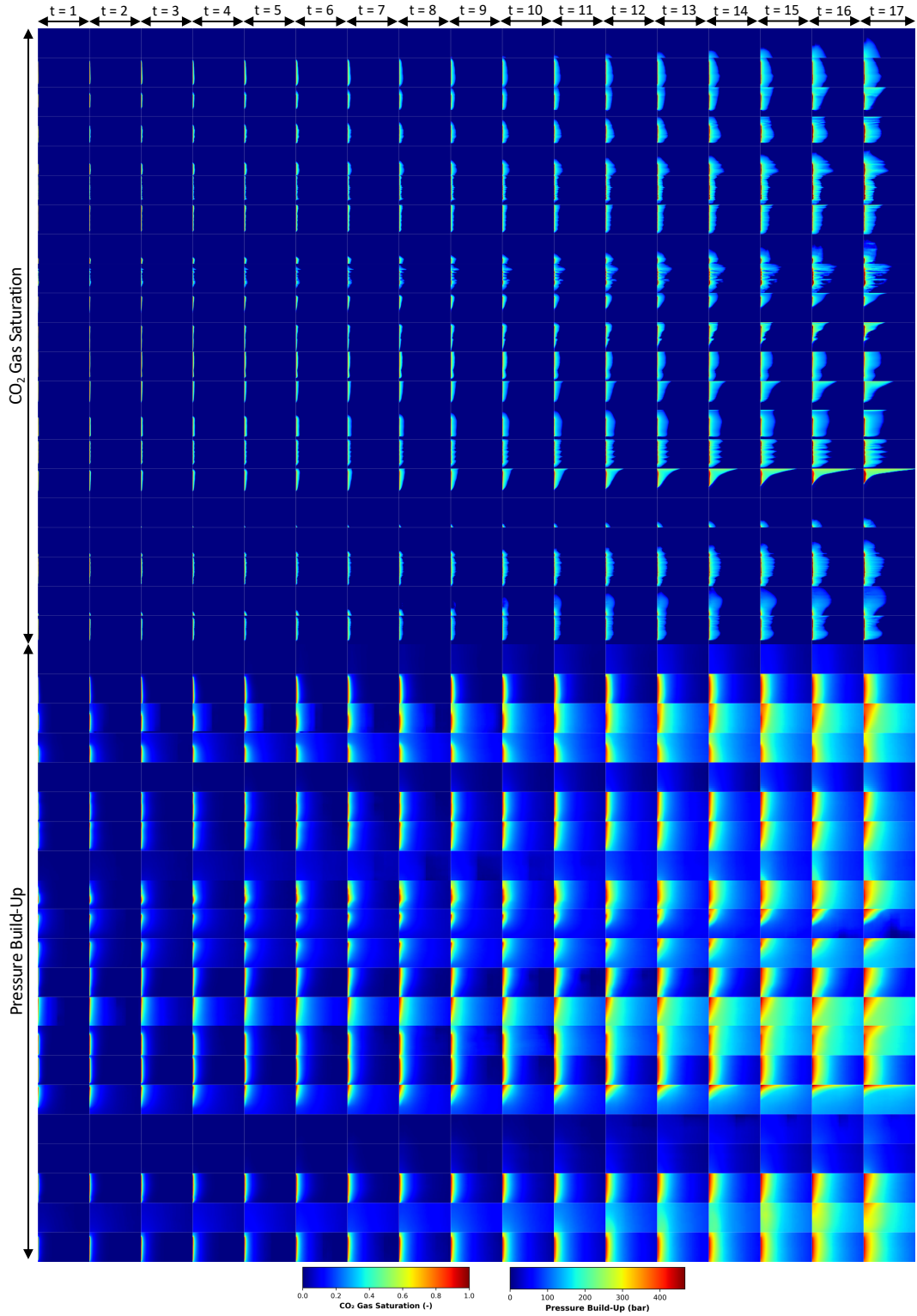


Figure 4. 21 unconditionally generated videos from the VDiT model (Stage II). The top 21 rows show CO₂ gas saturation field across 17 frames; the next 21 rows show the corresponding pressure build-up field, respectively.

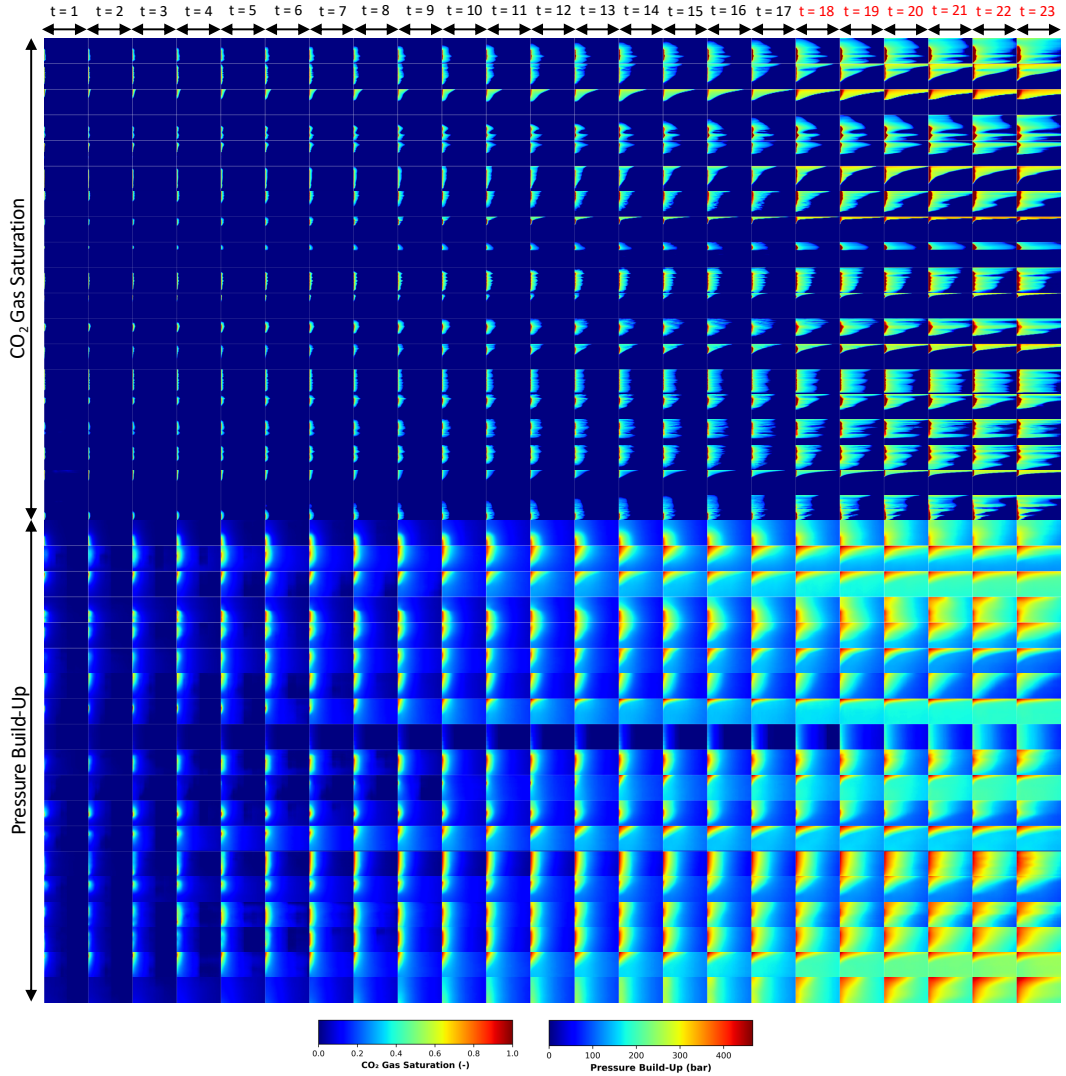


Figure 5. 19 unconditionally generated videos using the autoregressive strategy (Stage III). The top 19 rows show CO₂ gas saturation across 23 frames; the next 19 rows show the corresponding pressure build-up, respectively. Labels for frames 18–23 (beyond the 17-frame training horizon) are shown in red.

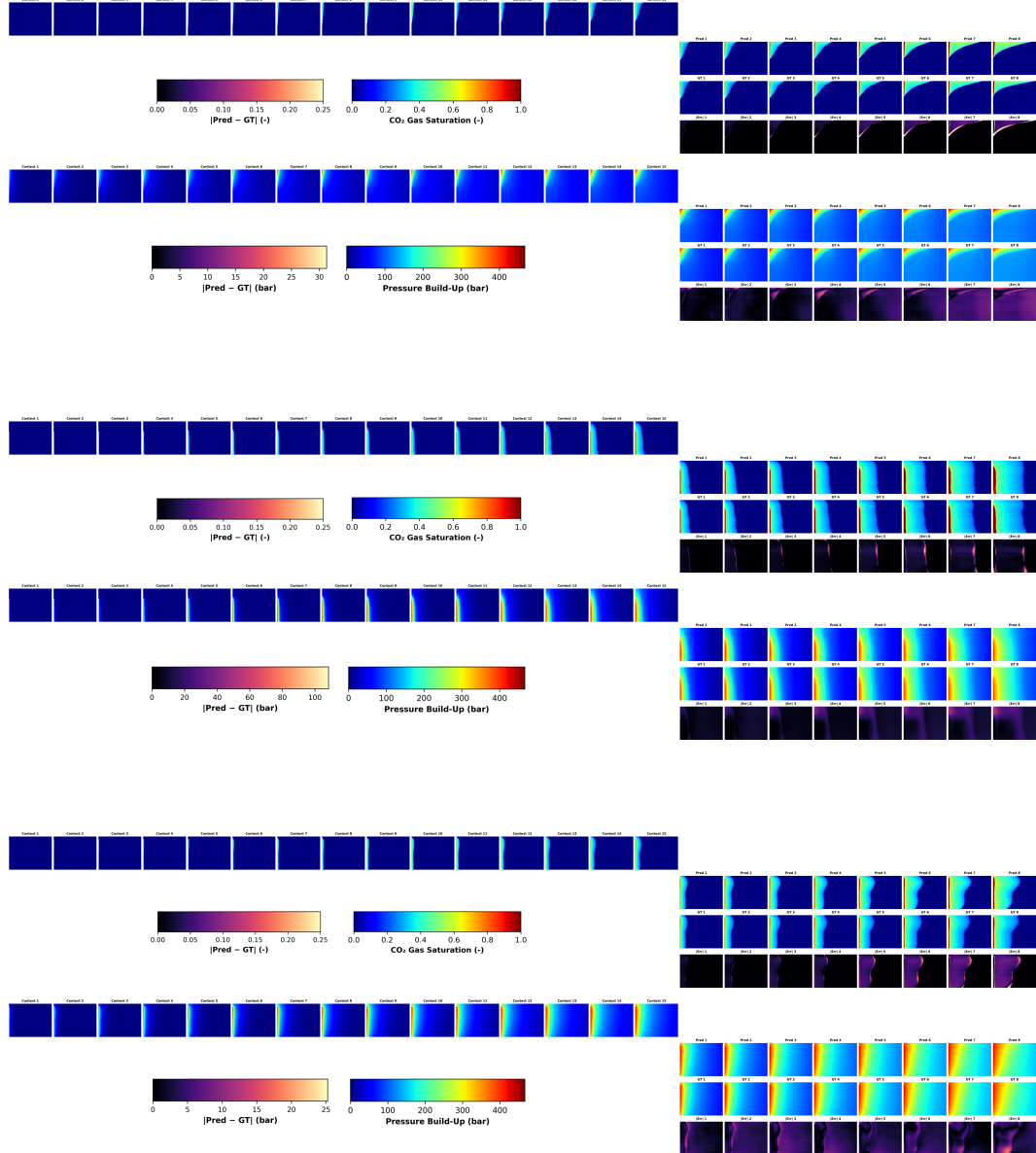


Figure 6. 3 conditionally sampled videos using $F_c = 15$ context frames from the validation set (Stage III inference). Each case includes the total $F_p = 8$ predicted frames, the corresponding ground truth, and the absolute error between them.

rates) to guide generation and to test whether the model can forecast for specified injection scenarios.

Lastly, the pre-training stage (Stage II) is costly, taking about 3 days to complete. Mixed precision and batch size strongly affect memory use and computational cost: higher precision increases memory use and smaller batches increase runtime. We trained the VQ-VAE and VAE in full precision (float32) with batch size 4. On top of these latent representations we pre-train and fine-tune the VDiT in lower precision (float16), with patch size 2, batch size 4 for pre-training, and batch size 2 for fine-tuning. To reduce memory and speed up runtime, we can move the autoencoders to lower precision (e.g., bfloat16 or float16), increase batch sizes, and increase patch size to cut the number of tokens. Finding the right configuration requires some tuning: for instance, increasing the patch size can reduce spatial resolution, and increasing the batch size can destabilize optimization or hurt generalization.

7 Conclusion

We presented LAViG-FLOW, a latent autoregressive video generation diffusion model that learns the coupled evolution of CO₂ gas saturation and pressure build-up in multiphase flow scenarios. It learns their joint distribution and generates high-resolution videos showing their combined evolution; with autoregressive fine-tuning, it extends the learned horizon from length F to F' , demonstrating forecasting ability. On the CO₂ sequestration dataset, the model generates videos of varying lengths in a short time. By contrast, on the same dataset, ECLIPSE simulations on an Intel® Xeon® Processor E5-2670 CPU use a dedicated core per run and require about 10 minutes (600 seconds) to produce a 24-frame video sample.

Open Research

The CO₂ geological sequestration simulation dataset used for training and evaluation can be downloaded from the public repository at https://drive.google.com/drive/folders/1fZQfMn_vsjKUXAfRV0q_gswt18JEkVGo?usp=sharing (Wen et al., 2022a), and its generation procedure is described by Wen et al. (2022b). The LAViG-FLOW training and inference code, together with the trained checkpoints, will be released at <https://github.com/DeepWave-KAUST/LAViG-FLOW-pub> after the final publication. The full pipeline is implemented in Python, and all figures shown in this manuscript were generated using Matplotlib 3.9.4 (Hunter, 2007).

Acknowledgments

This publication is based on work supported by the King Abdullah University of Science and Technology (KAUST). The authors gratefully acknowledge the support of the Deep-Wave sponsors and the computational resources provided by KAUST’s high-performance computing facilities. Special thanks are extended to the developers of the GCS open-source dataset used in this study.

Conflicts of Interest

The authors declare there are no conflicts of interest for this manuscript.

References

Babaeizadeh, M., Saffar, M. T., Nair, S., Levine, S., Finn, C., & Erhan, D. (2021). Fitvid: Overfitting in pixel-level video prediction. *arXiv preprint arXiv:2106.13195*.

Bachu, S. (2008). Co2 storage in geological media: Role, means, status and barriers to deployment. *Progress in Energy and Combustion Science*, 34(2), 254–273.

Blattmann, A., Dockhorn, T., Kulal, S., Mendelevitch, D., Kilian, M., Lorenz, D., ... others (2023). Stable video diffusion: Scaling latent video diffusion models to large datasets. *arXiv preprint arXiv:2311.15127*.

Blattmann, A., Rombach, R., Ling, H., Dockhorn, T., Kim, S. W., Fidler, S., & Kreis, K. (2023). Align your latents: High-resolution video synthesis with latent diffusion models. *arXiv preprint arXiv:2304.08818*.

Chen, J., Li, W., Zhang, P., Zhang, R., Liu, Z., & Qiao, Y. (2024). Ditpainter: Efficient video inpainting with diffusion transformers. In *Computer vision and pattern recognition workshops*.

Diab, W., & Al Kobaisi, M. (2024). U-deeponet: U-net enhanced deep operator network for geologic carbon sequestration. *Scientific Reports*, 14(1), 21298.

Dosovitskiy, A., Beyer, L., Kolesnikov, A., Weissenborn, D., Zhai, X., Unterthiner, T., ... Houlsby, N. (2021). An image is worth 16×16 words: Transformers for image recognition at scale. In *International conference on learning representations (iclr)*. Retrieved from <https://doi.org/10.48550/arXiv.2010.11929> doi: 10.48550/arXiv.2010.11929

Gan, M., Nguyen, M. C., Zhang, L., Wei, N., Li, J., Lei, H., ... Stauffer, P. H. (2021). Impact of reservoir parameters and wellbore permeability uncertainties on co2 and brine leakage potential at the shenhua co2 storage site, china. *International Journal of Greenhouse Gas Control*, 111, 103443.

Goodfellow, I., et al. (2014). Generative adversarial nets. In *Neurips*.

He, Y., Yang, T., Zhang, Y., Shan, Y., & Chen, Q. (2022). Latent video diffusion models for high-fidelity long video generation. *arXiv preprint arXiv:2211.13221*.

Higgins, I., Matthey, L., Pal, A., Burgess, C., Glorot, X., Botvinick, M., ... Lerchner, A. (2017). β -vae: Learning basic visual concepts with a constrained variational framework. In *International conference on learning representations*.

Ho, J., Jain, A., & Abbeel, P. (2020). Denoising diffusion probabilistic models. *arXiv preprint arXiv:2006.11239*.

Ho, J., Salimans, T., Gritsenko, A., Chan, W., Norouzi, M., & Fleet, D. J. (2022a). Video diffusion models. In *Advances in neural information processing systems*.

Ho, J., Salimans, T., Gritsenko, A., Chan, W., Norouzi, M., & Fleet, D. J. (2022b). Video diffusion models. *arXiv preprint arXiv:2204.03458*.

Huang, H.-P., Zhou, Y., Wang, J.-H., Liu, D., Liu, F., Yang, M.-H., & Xu, Z. (2024). Move-in-2d: 2d-conditioned human motion generation. *arXiv preprint arXiv:2412.13185*.

Huang, X., Wang, F., & Alkhalifah, T. (2024). *Diffusion-based subsurface co2 multiphysics monitoring and forecasting* (Tech. Rep.). King Abdullah University of Science and Technology.

Hunter, J. D. (2007). Matplotlib: A 2d graphics environment. *Computing in Science & Engineering*, 9(3), 90–95. doi: 10.1109/MCSE.2007.55

Jin, P., Meng, S., & Lu, L. (2022). Mionet: Learning multiple-input operators via tensor product. *SIAM Journal on Scientific Computing*, 44(6), A3490–A3514.

Johnson, J., Alahi, A., & Fei-Fei, L. (2016). Perceptual losses for real-time style transfer and super-resolution. *arXiv preprint arXiv:1603.08155*. Retrieved from <https://doi.org/10.48550/arXiv.1603.08155> doi: 10.48550/arXiv.1603.08155

Kim, B., Lee, K., Jeong, I., Cheon, J., Lee, Y., & Lee, S. (2025). On-device sora: Enabling training-free diffusion-based text-to-video generation for mobile devices. *arXiv preprint arXiv:2502.04363v2*. Retrieved from <https://doi.org/10.48550/arXiv.2502.04363> doi: 10.48550/arXiv.2502.04363

Kingma, D. P., & Welling, M. (2022). Auto-encoding variational bayes. *arXiv preprint arXiv:1312.6114*.

Krevor, S., Blunt, M. J., Benson, S. M., Pentland, C. H., Reynolds, C., Al-Menhali, A., & Niu, B. (2015). Capillary trapping for geologic carbon dioxide storage – from pore scale physics to field scale implications. *International Journal of Greenhouse Gas Control*, 40, 221–237.

Lee, H., Jang, Y., Jung, W., & Sung, W. (2016). Co₂ plume migration with gravitational, viscous, and capillary forces in saline aquifers. In *Volume 8: Polar and arctic sciences and technology; petroleum technology, american society of mechanical engineers* (p. V008T11A001). Busan, South Korea.

Liu, J., Yang, Y., Xu, Y., Zhang, Q., Liu, Z., & Qiao, Y. (2024). Harp: Autoregressive latent video prediction. *arXiv preprint arXiv:2406.11125*.

Liu, M., Chen, J., Chang, S., & Liu, Y. (2023). Flow straight and fast: Training continuous normalizing flows via rectified flow matching. In *International conference on learning representations*.

Liu, X., Gong, C., & Liu, Q. (2022). Flow straight and fast: Learning to generate and transfer data with rectified flow. *arXiv preprint arXiv:2209.03003*. Retrieved from <https://doi.org/10.48550/arXiv.2209.03003> doi: 10.48550/arXiv.2209.03003

Ma, X., Wang, Y., Chen, X., Jia, G., Liu, Z., Li, Y.-F., ... Qiao, Y. (2024). Latte: Latent diffusion transformer for video generation. In *Advances in neural information processing systems*.

Nordbotten, J. M., Flemisch, B., Gasda, S., Nilsen, H., Fan, Y., Pickup, G., ...

Pruess, K. (2012). Uncertainties in practical simulation of co₂ storage. *International Journal of Greenhouse Gas Control*, 9(3), 234–242.

Peebles, W., & Xie, S. (2022). Scalable diffusion models with transformers. In *Iccv*.

Pruess, K., Oldenburg, C., & Moridis, G. (1999). *Tough2 user's guide version 2, tech. rep., lawrence berkeley national lab. (lbnl)* (Tech. Rep.). Lawrence Berkeley National Laboratory.

Saadatpoor, E., Bryant, S. L., & Sepehrnoori, K. (2010). New trapping mechanism in carbon sequestration. *Transport in Porous Media*, 82(1), 3–17.

Tariq, Z., Ali, M., Yan, B., Sun, S., Khan, M., Yekeen, N., & Hoteit, H. (2023). Data-driven machine learning modeling of mineral/co₂/brine wettability prediction: Implications for co₂ geo-storage. In *Middle east oil, gas and geosciences show* (p. D011S033R005).

van den Oord, A., Vinyals, O., & Kavukcuoglu, K. (2017). Neural discrete representation learning. In *Advances in neural information processing systems (neurips)*.

Weissenborn, D., Täckström, O., & Uszkoreit, J. (2020). Scaling autoregressive video models. In *International conference on learning representations (iclr)*.

Wen, G., Li, Z., Azizzadenesheli, K., Anandkumar, A., & Benson, S. M. (2022a). *Co₂ geological sequestration simulation dataset* [Dataset].

Wen, G., Li, Z., Azizzadenesheli, K., Anandkumar, A., & Benson, S. M. (2022b). U-fno—an enhanced fourier neural operator-based deep-learning model for multiphase flow. *Advances in Water Resources*, 163, 104180.

Zhang, R., Isola, P., Efros, A. A., Shechtman, E., & Wang, O. (2018). The unreasonable effectiveness of deep features as a perceptual metric. In *Proceedings of the ieee/cvpr conference on computer vision and pattern recognition (cvpr)*.

Zhang, Y., Liu, S., Chen, Y., Zhang, Y., Liu, Z., & Qiao, Y. (2024). Progressive autoregressive video diffusion models. In *Advances in neural information processing systems*.

Zhao, M., Gerritsma, M., & Hajibeygi, H. (2023). Efficient simulation of co₂ migration dynamics in deep saline aquifers using a multi-task deep learning technique with consistency. *Advances in Water Resources*, 178, 104494.